RSC Advances

PAPER

View Article Online
View Journal | View Issue

Cite this: *RSC Adv.*, 2024, **14**, 19264

Liquid-phase xylene isomerization on nano-sized ZSM-5

Peixi Feng, Chenglin Kang,* Xin Yue, Zhenhuan Zhou, Zhongxun Liu, Yueting Gai, Junjun Shi and Baoning Zong

The isomerization process of xylene in the liquid phase has garnered significant attention due to its low energy consumption and high selectivity. However, conventional ZSM-5 zeolites have exhibited significantly diminished activity in this process, primarily attributed to diffusion barriers. To address this issue, Nano-ZSM-5 zeolite was synthesized using tetrapropylammonium hydroxide (TPAOH) as a structure direct agent (SDA) and introducing silicate-1 (S-1) as a crystallization seed. The impact of OH^-/SiO_2 molar ratio on the sample morphology was investigated. The structure of Nano-ZSM-5 zeolite was characterized by X-ray diffraction (XRD), scanning electron microscopy (SEM), transmission electron microscopy (TEM), and N_2 physical -sorption analysis. The results demonstrate that the addition of S-1 crystal seeds enables the formation of ZSM-5 crystallites with diminutive particle sizes (~20 nm). Furthermore, variations in the OH^-/SiO_2 molar ratio within the synthetic system impact crystallite aggregation, excessively high or low ratios result in severe aggregation, leading to decreased specific surface area and mesoporous volume. By optimizing the OH^-/SiO_2 molar ratio to 0.2, the sample exhibits exceptional dispersibility with a specific surface area of 420 $m^2\ g^{-1}$ and a mesoporous volume extending to 0.57 $cm^3\ g^{-1}$. When utilized as a catalyst for liquid-phase xylene isomerization, nano-ZSM-5 demonstrates superior catalytic performance compared to traditional zeolite.

Received 16th April 2024
Accepted 6th June 2024

DOI: 10.1039/d4ra02828g

rsc.li/rsc-advances

Introduction

Xylene is a crucial raw material in the petrochemical industry, and consists of three isomers: *o*-xylene (OX), *m*-xylene (MX), and *p*-xylene (PX).[1] Among these isomers, PX has the highest market demand due to its primary role as a raw material for polyester production.[2–4] The unit of xylene isomerization plays a significant role in the production of PX by converting OX and MX into PX.[5,6] However, this process also leads to the undesired side reaction known as xylene disproportionation, resulting in the formation of toluene and trimethylbenzene and causing loss of xylene.[7,8]

Xylene isomerization is typically catalyzed by Brønsted acids,[9–12] therefore, zeolite is deemed suitable for catalyzing this reaction.[13–16] ZSM-5 is a crucial high-silicon zeolite with a three-dimensional ten-membered annular channel structure. It exhibits high hydrothermal stability and strong acidity, making it extensively employed in various petrochemical applications such as fluid catalytic cracking, hydroisomerization, xylene isomerization, among others.[17] ZSM-5 is typically synthesized by incorporating quaternary ammonium salts as templates, such as tetraethylammonium hydroxide (TEAOH) and tetrapropylammonium hydroxide (TPAOH).[18] ZSM-5 synthesized using a single template agent generally exhibits a larger particle size, ranging from several hundred nanometers to microns.[19] The conventional gas-phase xylene isomerization process employing ZSM-5 zeolite is typically synthesized utilizing a single template agent. This gas-phase approach requires higher reaction temperatures and lower reaction pressures. In contrast, the liquid-phase xylene isomerization process occurs at lower temperatures and relatively higher pressures, resulting in significant energy savings compared to the gas phase process. Furthermore, owing to the constraint of low temperature on the side reaction of disproportionation, the liquid phase process exhibits remarkable selectivity.[20–22] However, direct application of ZSM-5 zeolite used in the gas phase process to the liquid phase reaction limits the activity due to reduced molecular diffusion rates under liquid phase conditions. This hinders full contact between the liquid reactants and active sites on the catalyst.[23–25] To overcome these diffusion problems, hierarchical porous zeolites have been widely employed in recent years.[26–28] There are primarily two preparation strategies for hierarchical porous zeolite. One approach involves the synthesis of zeolites with combined micropores and mesopores, typically achieved through post-treatment or the addition of a mesoporous templating agent to the synthesis system.[29–37] The other strategy focuses on synthesizing zeolites with small particle sizes, which tend to agglomerate and form numerous intergranular mesopores.[38–40] The seed induction method represents an effective approach for synthesizing nano-ZSM-5, offering advantages such as reduced the usage of SDAs and rapid crystallization

Research Institute of Petroleum Processing, SINOPEC, Beijing, 100083, PR China. E-mail: kangcl.ripp@sinopec.com

rate.[41,42] Nano-sized ZSM-5 was synthesized by Nada and coworks[43] through the addition of crystal seeds without the use of any structure direct agent (SDA). The crystal seeds utilized were ZSM-5 zeolite with an average particle size of approximately 70 nm. The impact of various synthesis conditions on zeolite morphology were investigated, revealing that synthesis temperature and crystallization time exerted the most significant influence, followed by alkalinity and seed particle size. By precisely controlling these synthesis conditions, it is possible to synthesize small-grained zeolite with uniform particles even in the absence of SDAs. Zhang *et al.*[44,45] developed a "salt-aided seed-induced route" method for synthesizing nano-ZSM-5 by incorporating silicate-1 (S-1) zeolite as a seed in the synthetic system. They employed tetrapropylammonium bromide (TPABr) as SDA and observed that the addition of KF salt resulted in reduced crystallization time, decreased template agent quantity, and expanded Si/Al ratio range of the zeolite. By precisely controlling the amount of KF salt in the synthesis system, they achieved more accurate regulation of mesopore aperture and volume. Chen *et al.*[46] synthesized ZSM-5 zeolite aggregates with a well-developed mesoporous structure by utilizing S-1 zeolite as a crystal seed and employing TPAOH and cetyltrimethylammonium bromide (CTAB) as SDA. It was observed that the addition of CTAB effectively inhibited the secondary growth of zeolite, thereby facilitating the formation of nano-ZSM-5 aggregates. Moreover, an increase in the quantity of S-1 seed led to the generation of smaller primary crystals.

In this work, nanosized ZSM-5 was synthesized using TPAOH as a SDA and S-1 zeolite as a crystal seed. The influence of OH^-/SiO_2 on sample morphology was investigated. The structure of the nano-ZSM-5 was characterized by scanning electron microscopy (SEM), transmission electron microscopy (TEM), X-ray diffraction (XRD), and N_2 physical sorption analysis. NH_3 programmed temperature desorption (NH_3-TPD) was employed to investigate acidity. Notably, the nanometer-sized ZSM-5 zeolite exhibited superior activity compared to traditional microporous counterpart in liquid-phase xylene isomerization.

Experimental

Synthesis of S-1 seed

The S-1 seed was synthesized following the procedure described in ref. 47. 14.95 g of deionized H_2O, 5.08 g of TPAOH (40 wt% in water), and 9.2 g of ethanol (EtOH, Ar) were thoroughly mixed for 1 h. Subsequently, with continuous stirring, 10.42 g of TEOS(Ar) was slowly added to the mixture, which was then stirred and aged for 2 h. The molar ratio of the materials was $20H_2O : 0.2TPAOH : 8EtOH : SiO_2$. The mixture was transferred into a Teflon-lined autoclave and hydrothermally treated at 140 °C for 72 hours. The product was filtered and washed with deionized water, dried at 120 °C for 6 h followed by calcined at 550 °C for 6 h. The obtained S-1 zeolite was used as the crystal seeds for subsequent experiments.

Synthesis of the nano-zeolite

Nano-ZSM-5 zeolite was prepared using S-1 as crystal seed, fumed silica as silicon source, $NaAlO_2$ (Ar) as aluminum source, OH^-/SiO_2 molar ratio was regulated by NaOH (Ar). 0.164 g $NaAlO_2$, 0.12 g NaOH, 0.9 g S-1 seed, 30.87 g deionized water, 2.54 g TPAOH(40 wt% in water) were thoroughly mixed for 1 h. Subsequently, 6 g fumed silica was gradually added to the mixture under continuous stirring followed by stirring and aging for 2 h. The molar ratio of the material was $20H_2O : 0.15S\text{-}1 : 0.05TPAOH : 0.1OH^- : 0.01Al_2O_3 : SiO_2$, and then the mixture is transferred into a Teflon-lined autoclave and hydrothermally treated at 170 °C for 36 hours. The product was filtered and washed with deionized water, dried at 120 °C for 6 h followed by calcined at 550 °C for 6 h to obtain nano-NaZSM-5. Ion exchange was carried out with 1 mol per L NH_4Cl solution at 90 °C, then filtered, washed and dried. HZSM-5 was obtained by calcination at 500 °C for 6 h. In order to investigate the influence of OH^-/SiO_2 on zeolite morphology, the OH^-/SiO_2 ratio in the synthetic system was varied to 0.15, 0.2, and 0.25 by adjusting the amount of NaOH added. The resulting zeolite samples were denoted as Z-N-*x*, where *x* represents the corresponding OH^-/SiO_2 molar ratio which was 0.1, 0.15, and 0.2 respectively. For comparison, ZSM-5 zeolite was synthesized under identical conditions and procedures without the addition of seed or TPAOH, and the molar ratio of OH^-/SiO_2 was adjusted to 0.2, resulting in samples denoted as Z-N-S and Z-N-T respectively.

Catalyst characterizations

XRD patterns of the samples were obtained by CuKα radiation on Rigaku D/MAX-IIIA, the tube voltage is 40 kV and the current is 40 mA. The relative crystallinity is determined by integrating the peak areas between 22.5° and 25.0°. The sample with the largest peak area is designated as the reference sample, with a relative crystallinity of 100%. The relative crystallinity of other samples is calculated as the ratio of their peak area to that of the reference sample. The pore and specific surface area of the samples were tested by nitrogen sorption measurements at −196 °C on Micromeritics ASAP 2020. Each sample was analyzed after 8 h degassed at 350 °C. The total surface area was calculated by the Brunauer–Emmett–Teller (BET) equation, and the total pore volume was determined at $p/p_0 = 0.99$. The micropore surface area and the micropore volume were calculated by the *t*-plot method. The scanning electron microscope (SEM) images were taken on the Hitachi SU-8010, and the operating voltage was 5 kV. The transmission electron microscope (TEM) images were taken by JEOL JEM-2100 electron microscope with the acceleration voltage of 200 kV. Elemental analysis of samples were performed using X-ray fluorescence (XRF) on Rigaku ZSX100E X-ray fluorescence spectrometer instrument. Acidity of samples were characterized by temperature-programmed desorption of ammonia (NH_3-TPD) which was performed on the Micromeritics AutoChem II 2920. The sample was heated to 600 °C in He atmosphere for 1 h. After cooling to 100 °C, the system was switched to a mixture of 10% NH_3–He mixture and the NH_3 was adsorbed until saturation for 1 h. Subsequently, the system was switched back to He and heated again up to 600 °C at a rate of 10 °C min^{-1}. Data was collected by the thermal conductivity detector (TCD). The quantification of weakly acidic and strongly acidic sites was

performed through the integration of NH_3-TPD curve and standard curve analysis.

Catalytic tests

The liquid phase xylene isomerization was conducted in a fixed bed reactor with an inner diameter of 6 mm and a length of 750 mm. The sample was compressed and fractured, and then 20–40 mesh particles were screened for experiment. The catalyst loading was 0.5 g. The molar composition of the reaction mixture was MX : OX = 3 : 2. The Weight hourly space velocity (WHSV) was set at 6 h^{-1}, while the reaction temperature and pressure were maintained at 260 °C and 2 MPa, respectively.

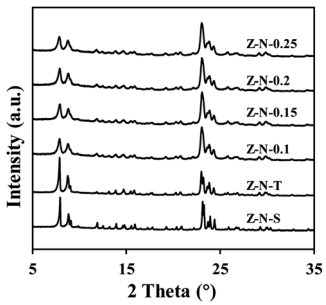

Fig. 1 XRD patterns of all ZSM-5 samples.

The reaction product was analyzed by online gas phase chromatograph using Agilent 7890A which equipped with a HP-WAX column (60 m × 0.25 mm × 0.5 μm) and a FID detector.

The catalyst activity was determined by the ratio of PX in the product to the total xylene content, which can be calculated using the following formula:

$$\mathrm{PX/X}(\%) = W_{\mathrm{PX}}/W_{\mathrm{X}} \times 100$$

where W_{PX} is the amount of PX in the product, W_{X} is the total amount of xylene in the product. Owing to the thermodynamic equilibrium limitation, the highest proportion of PX in xylene mixture is about 24%. The selectivity of the catalyst was determined by yield of xylene X_y, which was calculated by the ratio of the total xylene in the product to the total xylene in the reactant:

$$X_y(\%) = W_{\mathrm{Xo}}/W_{\mathrm{Xi}} \times 100$$

where W_{Xo} is the total amount of xylene in the product, W_{Xi} is the total amount of xylene in the reactant.

Results and discussion

Characterization of the ZSM-5 samples

The XRD pattern of samples are presented in Fig. 1, revealing the characteristic peak of ZSM-5 zeolite for all samples. The crystallinity of Z-N-S is determined to be 100%, while the

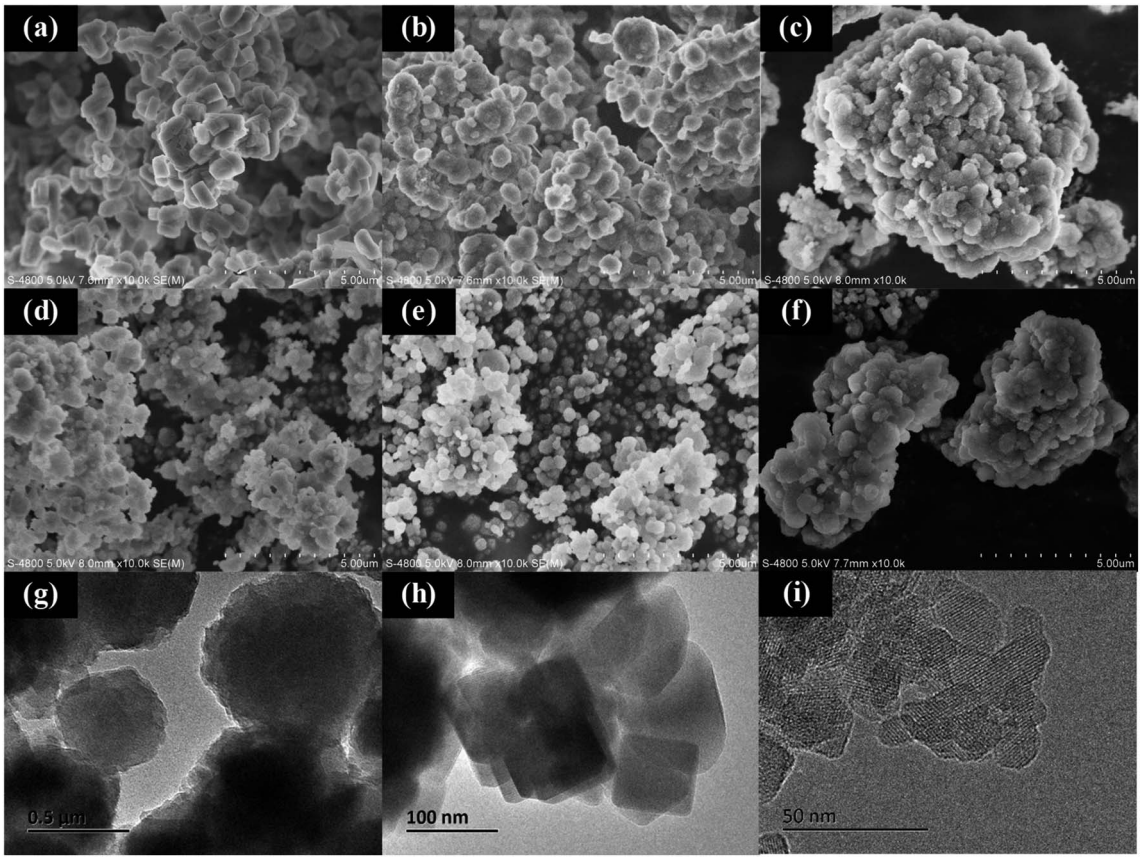

Fig. 2 SEM images of Z-N-S (a), Z-N-T (b), Z-N-0.1 (c), Z-N-0.15 (d), Z-N-0.2 (e), Z-N-0.25 (f) and TEM images of Z-N-S (g), Z-N-T (h), Z-N-0.2 (i).

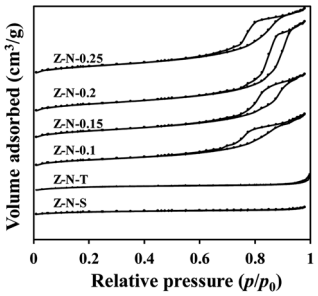

Fig. 3 N_2 adsorption–desorption isotherms of ZSM-5 samples.

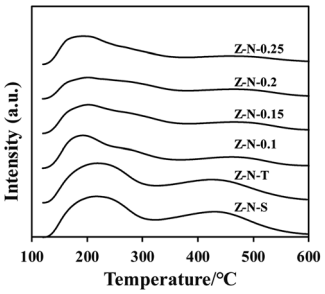

Fig. 4 NH_3-TPD curves of ZSM-5 samples.

relative crystallinity for Z-N-T and Z-N-x ($x \sim 0.1, 0.15, 0.2, 0.25$) are 91.5%, 68.5%, 71.4%, and 70.2% respectively. Notably, the crystallinity of Z-N-x sample is comparatively lower than that of the other two samples, accompanied by a noticeable broadening phenomenon in the XRD pattern peaks, indicating smaller particle size for Z-N-x zeolite.

The SEM and TEM images of the sample are presented in Fig. 2. It can be observed that Z-N-S particles exhibit a bulk morphology with an average size of approximately 500 nm, while Z-N-T particles display a spherical shape with a similar size range. Notably, as depicted in Fig. 2g–i, the single crystal size of the Z-N-0.2 sample are found to be significantly smaller, measuring around 20 nm. Furthermore, Fig. 2c–f reveal that at lower OH^-/SiO_2 ratios within the synthetic system, there is a pronounced tendency for nano-zeolite agglomeration, the agglomeration effect weakens as the OH^-/SiO_2 ratio increases. When the OH^-/SiO_2 ratio reaches 0.25, zeolite agglomeration reoccurs, indicating that both excessively low and high OH^-/SiO_2 ratios can lead to severe particle clustering.

Fig. 3 shows the N_2 adsorption–desorption isotherms of each sample. It can be observed that Z-N-T and Z-N-x samples exhibit type IV absorption/desorption isotherms with hysteresis loops, while the hysteresis loops of Z-N-x are more pronounced, indicating a greater amount of mesoporous in Z-N-X samples. In contrast, Z-N-S sample displays type I absorption/desorption isotherms without hysteresis loops, suggesting an absence of mesoporous pores.

The textural properties of each sample are summarized in Table 1. The SiO_2/Al_2O_3 of samples are determined by XRF. The data indicate that Z-N-x samples exhibit a higher degree of mesoporosity compared to Z-N-S and Z-N-T samples. Notably, when the OH^-/SiO_2 molar ratio in the synthesized system is set at 0.2, the resulting sample demonstrates the largest specific surface area and mesoporous volume, which aligns with observations made through SEM analysis. Therefore, an OH^-/SiO_2 ratio of 0.2 appears to be more suitable.

Table 1 Textural properties of the ZSM-5 samples

		Specific surface area/($m^2\ g^{-1}$)			Pore volume/($cm^3\ g^{-1}$)		
Sample	SiO_2/Al_2O_3	Total	Micro	Meso	Total	Micro	Meso
Z-N-S	98.3	353.26	334.71	18.55	0.19	0.15	0.04
Z-N-T	99.2	396.21	338.11	58.10	0.29	0.15	0.14
Z-N-0.1	94.1	363.35	212.21	151.14	0.44	0.10	0.34
Z-N-0.15	92.3	405.83	241.72	164.11	0.52	0.11	0.41
Z-N-0.2	93.5	420.19	249.02	171.17	0.68	0.11	0.57
Z-N-0.25	94.3	403.86	207.73	196.13	0.53	0.09	0.44

Table 2 Acid properties of ZSM-5 samples

	Acid amount (mmol g^{-1})		
Samples	Weak	Strong	Total
Z-N-S	0.355	0.302	0.657
Z-N-T	0.342	0.294	0.636
Z-N-0.1	0.282	0.142	0.424
Z-N-0.15	0.261	0.135	0.396
Z-N-0.2	0.221	0.115	0.336
Z-N-0.25	0.256	0.121	0.377

The NH_3-TPD curves of each sample were presented in Fig. 4, revealing two distinct NH_3 desorption peaks near 200 °C and 450 °C, corresponding to weak acid sites and strong acid sites, respectively. The acid content was summarized in Table 2. Notably, the acid content of Z-N-X was found to be lower than that of Z-N-T and Z-N-S samples, indicating a reduction in nano-zeolite acidity attributed to decreased crystallinity.

Catalytic performance on liquid phase isomerization

The catalytic performance of Z-N-S, Z-N-T, and Z-N-0.2 samples was evaluated at 260 °C, 2 MPa, and a WHSV of 6 h^{-1}, respectively. The results are presented in Fig. 5. The reaction features of the three catalysts remained essentially unchanged within a period of 30 h, indicating their high stability. Among these catalysts, Z-N-0.2 exhibited the highest activity with PX/X reaching approximately 22.5%. However, its xylene yield was comparatively lower due to increased side reaction activity. It can be observed from Table 2 that despite having the lowest acid content among the three catalysts, Z-N-0.2 displayed the highest catalytic activity. This suggests that diffusion hinders prevent the reaction and the presence of mesoporous pores effectively eliminates diffusion resistance thereby enhancing the catalyst activity.

In order to investigate the catalytic performance of the Z-N-0.2 sample under different conditions, variations in reaction temperature and WHSV were implemented, as depicted in Fig. 6. As the WHSV increases, the contact time between

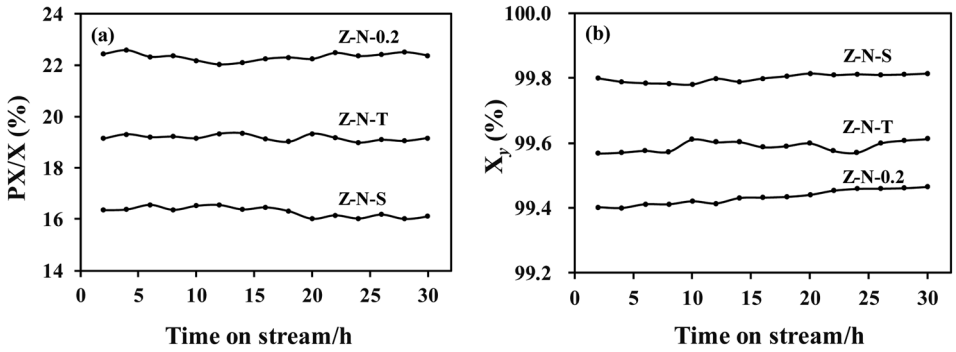

Fig. 5 Liquid phase xylene isomerization activity (a) and selectivity (b) of three samples.

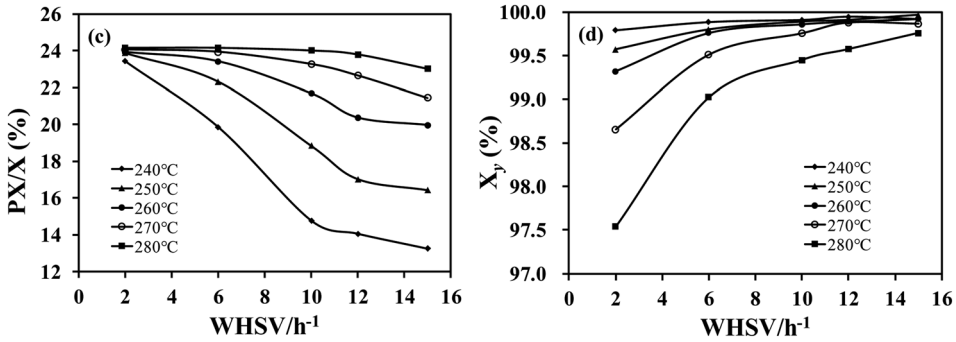

Fig. 6 Liquid phase xylene isomerization activity (c) and selectivity (d) of Z-N-0.2 sample under different conditions.

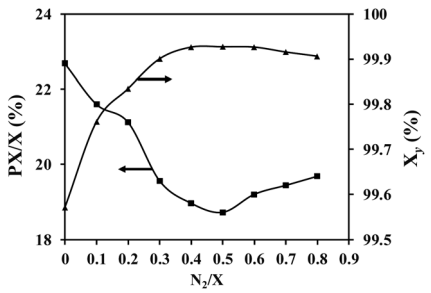

Fig. 7 Impact of N_2 to reactant xylene molar ratio on catalyst activity and selectivity.

reactants and catalyst decreases, resulting in a gradual decline in catalytic activity. However, at higher reaction temperatures, the impact of increased WHSV on activity becomes less pronounced. Notably, even with higher WHSV above 270 °C, catalytic activity can still be maintained at elevated levels. Furthermore, when operating at a WHSV of 2 h^{-1}, lower temperatures can ensure both high catalytic activity and favorable xylene yield. Specifically, at 250 °C, PX/X reaches 23.7% while X_y exceeds 99.5%, surpassing reported literature[48,49] values.

The diffusion of reactants in the liquid phase process has been identified as a significant factor impeding catalyst activity. To mitigate the impact of diffusion on catalyst performance, it is proposed to introduce a certain amount of inert gas into the reactor. N_2 was employed as the inert gas, with its quantity calculated based on the molar ratio of N_2 to xylene (N_2/X). The catalytic performance of the catalyst under different N_2/X molar ratio was evaluated at 250 °C temperature, 2.5 MPa pressure, and 10 h^{-1} WHSV, as depicted in Fig. 7. The figure demonstrates that the addition of a small quantity of N_2 enhances the apparent activity of the catalyst. However, it also accelerates side reactions, leading to a decrease in xylene yield. The introduction of inert gas can enhance liquid turbulence, thereby inducing the transition from laminar flow to turbulent flow in the liquid material. Turbulence facilitates a reduction in the thickness of the mass transfer boundary layer, thus promoting enhanced contact between reactive materials and catalyst active sites. Increasing the amount of inert gas introduced leads to a higher degree of turbulence in the liquid material and a smaller diffusion boundary layer thickness. At an N_2/X molar ratio of approximately 0.4, the catalyst's activity reaches maximum, indicating that diffusion no longer significantly influences catalytic performance at this point. Further increase in N_2/X ratio (around 0.7) causes a decline in catalyst activity due to excessive N_2 content resulting in reduced xylene partial pressure within the liquid phase range. Hence, it can be inferred that introducing inert gas is an effective approach for mitigating diffusion effects.

Conclusions

The nanosized ZSM-5 was synthesized using TPAOH as a SDA and silicate-1 zeolite as a crystal seed, resulting in the formation

of ZSM-5 particles with an average crystal size of approximately 20 nm. The agglomeration of the zeolite in the synthetic system was influenced by the OH^-/SiO_2 molar ratio, where excessively high or low alkalinity led to severe agglomeration, thereby reducing both specific surface area and mesopore volume. Optimal dispersion of the sample was achieved when maintaining an OH^-/SiO_2 molar ratio of 0.2 in the synthetic system. Compared to traditional ZSM-5 zeolite catalysts, the nano-sized ZSM-5 zeolite exhibited enhanced catalytic activity for liquid-phase xylene isomerization. To mitigate diffusion effects during liquid-phase reactions, inert gas (N_2) injection into the reactor was employed to enhance turbulence and improve catalytic performance. It was observed that injecting a small amount of N_2 into the reactor increased the apparent activity of the catalyst, indicating that inert gas injection is an effective method for eliminating diffusion in liquid phase reactions. The high activity and stability of ZSM-5 in liquid-phase xylene isomerization, coupled with its lower reaction temperature and higher selectivity compared to gas-phase isomerization, render it highly promising for practical applications.

Conflicts of interest

There are no conflicts to declare.

Acknowledgements

We gratefully acknowledge the support from the China Petrochemical Corporation (Sinopec Group, 421108-4-4) on this work.

Notes and references

1 N. R. Demikhova, M. I. Rubtsova, V. A. Vinokurov and A. P. Glotov, *Pet. Chem.*, 2021, **61**, 1158–1177.
2 J. Hao, P. Feng, F. Xin, Z. Wang, Z. Zhou, D. Bao and Z. Zhu, *Chem. Eng. Sci.*, 2023, **268**, 118425.
3 G. Horacio, R. Abante, C. Luis and R. Jorge, *Ind. Eng. Chem. Res.*, 1996, **35**, 3964–3972.
4 Q. Shi, J. C. Gonçalves, A. F. Ferreira and A. E. Rodrigues, *Chem. Eng. Process.*, 2021, **169**, 108603.
5 M. Minceva, P. S. Gomes, V. Meshko and A. E. Rodrigues, *Chem. Eng. J.*, 2008, **140**, 305–323.
6 J. C. Goncalves and A. E. Rodrigues, *Chem. Eng. J.*, 2014, **258**, 194–202.
7 Y. Voloshina, L. Patrilyak, V. Ivanenko and K. Patrilyak, *Theor. Exp. Chem.*, 2009, **45**, 263–266.
8 X. Chang, Y. Li and Z. Zeng, *Ind. Eng. Chem. Res.*, 1992, **31**, 187–192.
9 M. Guisnet, N. S. Gnep and S. Morin, *Microporous Mesoporous Mater.*, 2000, **35**, 47–59.
10 Q. Shi, J. C. Gonçalves, A. F. Ferreira, M. G. Plaza and A. E. Rodrigues, *Ind. Eng. Chem. Res.*, 2018, **57**, 5568–5579.
11 A. Corma, A. Cortes, I. Nebot and F. Tomas, *J. Catal.*, 1979, **57**, 444.
12 A. Corma and E. Sastre, *J. Catal.*, 1991, **129**, 177–185.
13 S. A. Ali, A. M. Aitani, C. Ercan, Y. Wang and S. Al-Khattaf, *Chem. Eng. Res. Des.*, 2011, **89**, 2125–2135.
14 J. C. Gonçalves and A. E. Rodrigues, *Chem. Eng. Technol.*, 2013, **36**, 1658–1664.
15 E. R. Naranov, K. I. Dement Ev, I. M. Gerzeliev, N. V. Kolesnichenko, E. A. Roldugina and A. L. Maksimov, *Pet. Chem.*, 2019, **59**, 247–261.
16 A. M. Tarditi, G. I. Horowitz and E. A. Lombardo, *Catal. Lett.*, 2008, **123**, 7–15.
17 Z. Y Wu and Y. M. Wang, *Curr. Org. Chem.*, 2014, **18**, 1305–1322.
18 J. Wang, J. C. Groen, W. Yue, W. Zhou and M. Coppens, *J. Mater. Chem.*, 2008, **18**, 468–474.
19 S. Sang, F. Chang, Z. Liu, C. He, Y. He and L. Xu, *Catal. Today*, 2004, **93–95**, 729–734.
20 A. Iliyas and S. Al-Khattaf, *Chem. Eng. J.*, 2005, **107**, 127–132.
21 A. Iliyas and S. Al-Khattaf, *Ind. Eng. Chem. Res.*, 2004, **43**, 1349–1358.
22 J. C. Gonçalves and A. E. Rodrigues, *Chem. Eng. Technol.*, 2016, **39**, 225–232.
23 P. S. Sarma and S. Bhatia, *Zeolites*, 1987, **7**, 511–516.
24 U. K. Singh and M. A. Vannice, *Appl. Catal., A*, 2001, **213**, 1–24.
25 A. Mills, J. Wang and D. F. Ollis, *J. Phys. Chem. B*, 2006, **110**, 14386–14390.
26 S. Du, F. Li, Q. Sun, N. Wang, M. Jia and J. Yu, *Chem. Commun.*, 2016, **52**, 3368–3371.
27 X. Yang, L. Chen, Y. Li, J. C. Rooke, C. Sanchez and B. Su, *Chem. Soc. Rev.*, 2017, **46**, 481–558.
28 S. Du, Q. Sun, N. Wang, X. Chen, M. Jia and J. Yu, *J. Mater. Chem. A*, 2017, **5**, 7992–7998.
29 M. Choi, K. Na, J. Kim, Y. Sakamoto, O. Terasaki and R. Ryoo, *Nature*, 2009, **461**, 246–249.
30 H. S. Cho and R. Ryoo, *Microporous Mesoporous Mater.*, 2012, **151**, 107–112.
31 M. Zhang, L. Wang, Y. Chen, Q. Zhang and C. Liang, *J. Energy Chem.*, 2016, **25**, 539–544.
32 Y. Zhu, Z. Hua, J. Zhou, L. Wang, J. Zhao, Y. Gong, W. Wu, M. Ruan and J. Shi, *Chem.–Eur. J.*, 2011, **17**, 14618–14627.
33 Q. Yang, H. Zhang, M. Kong, X. Bao, J. Fei and X. Zheng, *Chin. J. Catal.*, 2013, **34**, 1576–1582.
34 A. Ates, *J. Colloid Interface Sci.*, 2018, **523**, 266–281.
35 X. Yang, X. Su, B. Liang, Y. Zhang, H. Duan, J. Ma, Y. Huang and T. Zhang, *Catal. Sci. Technol.*, 2018, **8**, 4338–4348.
36 X. Chen, R. Jiang, Y. Gao, Z. Zhou and X. Wang, *Crystengcomm*, 2021, **23**, 2793–2800.
37 B. Louis, F. Ocampo, H. Yun, J. Tessonnier and M. M. Pereira, *Chem. Eng. J.*, 2010, **161**, 397–402.
38 L. Frunz, R. Prins and G. D. Pirngruber, *Microporous Mesoporous Mater.*, 2006, **88**, 152–162.
39 J. Jin, L. Cao, Q. Hu, C. Xu, X. Gao, W. Feng, H. Liu and H. Liu, *J. Mater. Chem. A*, 2014, **2**, 7853–7861.
40 C. Fan, Y. Wang, H. Li, X. Wang, C. Sun, X. Zhang, C. Wang and S. Wang, *New J. Chem.*, 2018, **42**, 17043–17055.
41 R. Jain and J. D. Rimer, *Microporous Mesoporous Mater.*, 2020, **300**, 110174.

42 Q. Yu, Q. Zhang, J. Liu, C. Li and Q. Cui, *Crystengcomm*, 2013, **15**, 7680–7687.
43 M. H. Nada and S. C. Larsen, *Microporous Mesoporous Mater.*, 2017, **239**, 444–452.
44 H. Zhang, Z. Hu, L. Huang, H. Zhang, K. Song, L. Wang, Z. Shi, J. Ma, Y. Zhuang and W. Shen, *ACS Catal.*, 2015, **5**, 2548–2558.
45 H. Zhang, K. Song, L. Wang, H. Zhang, Y. Zhang and Y. Tang, *Chemcatchem*, 2013, **5**, 2874–2878.
46 H. Chen, Y. Wang, F. Meng, H. Li, S. Wang, C. Sun, S. Wang and X. Wang, *RSC Adv.*, 2016, **6**, 76642–76651.
47 F. Meng, Y. Wang, L. Wang, R. Yang and T. Zhang, *J. Mol. Catal. A: Chem.*, 2011, **335**, 105–111.
48 G. B. Kuzmanich, V. G. Deak and D. Y. Jan, *US Pat.*, 10927057B1, 2021.
49 J. E. Bauer, *US Pat.*, 7371913B2, 2008.